

Article

Properties of Fluorine-Free Steelmaking Flux Prepared Using Red Mud

Zheng Zhao, Yanling Zhang *  and Kan YuState Key Laboratory of Advanced Metallurgy, University of Science and Technology Beijing,
Beijing 100083, China

* Correspondence: zhangyanling@metall.ustb.edu.cn or ustbzly1108@163.com

Abstract: The basic oxygen steelmaking process is based on the CaO-FeO-SiO₂ ternary slag system, characterized by a high melting point and low lime dissolution rate, often becoming one of the key factors limiting the efficiency of the converter. The bulk solid waste red mud, produced by the Bayer alumina process and rich in Fe₂O₃/Al₂O₃/Na₂O, significantly reduces the melting point of the steelmaking slag system and enhances the efficiency of lime dissolution. This study utilized red mud as the main raw material to prepare a fluoride-free flux. An in situ online observation system was used to measure the melting point of the flux and the dissolution rate of lime in the flux. The results indicate that the melting point of the red mud-based flux is below 1200 °C, and under the same conditions, the lime dissolution rate is 10 to 15 times higher than when this flux is not used. Experiments in a 10 kg induction furnace show that using this flux, the dephosphorization rate under conditions without oxygen blowing is close to 40%, far higher than the rate achieved using CaF₂. Under oxygen-blowing conditions, the dephosphorization rate using the red mud-based flux is comparable to that of CaF₂, and significantly higher than without any flux, especially under high [C] content conditions. The data show that the red mud-based flux has the potential to be widely used as a fluoride-free flux in the steelmaking process.

Keywords: fluorine-free flux; steelmaking; lime dissolution; dephosphorization; red mud



Citation: Zhao, Z.; Zhang, Y.; Yu, K. Properties of Fluorine-Free Steelmaking Flux Prepared Using Red Mud. *Metals* **2024**, *14*, 315. <https://doi.org/10.3390/met14030315>

Academic Editor: Henrik Saxen

Received: 26 January 2024

Revised: 3 March 2024

Accepted: 5 March 2024

Published: 8 March 2024



Copyright: © 2024 by the authors. Licensee MDPI, Basel, Switzerland. This article is an open access article distributed under the terms and conditions of the Creative Commons Attribution (CC BY) license (<https://creativecommons.org/licenses/by/4.0/>).

1. Introduction

Rapid formation of liquid slag in the steelmaking process is key to improving smelting efficiency [1]. The melting point of lime is 2572 °C, and the key to rapidly forming liquid slag is to lower the melting point of lime. As shown in Figure 1, the addition of CaF₂ significantly lowers the melting point of lime and exhibits an excellent fluxing effect [2], but its use has been banned due to potential environmental hazards [3]. To enhance the efficiency of the converter in smelting, the development of low-melting-point, fluoride-free fluxes is significant. This is especially true under current blast furnace ironmaking conditions, which lead to lower silicon content in hot metal, insufficient heat in the converter, and extensive use of scrap steel [4].

Figure 1 shows that in addition to CaF₂, FeO and Al₂O₃ can also significantly lower the melting point of lime. Additionally, numerous studies have indicated that Na₂O effectively reduces the melting point and viscosity of slag and improves the phosphorus distribution ratio. In basic oxygen furnace steelmaking practice, early in the smelting process, adjustments in the oxygen blowing regime typically result in FeO content of 20% to 40% in the initial slag, which aids in lime melting and rapid formation of fluid liquid slag [5]. Ban-ya et al. [6] prepared a flux containing FeO and Al₂O₃, which achieved an 80% dephosphorization rate under 1350 °C silicon-free hot metal conditions, with an addition rate of 40 kg/t steel, attributed to the flux's rapid slagging and efficient utilization of lime; Ishikawa et al. [7] also obtained similar results. Li et al. [8] replaced CaF₂ with Al₂O₃ in hot metal dephosphorization slag, finding that with the increase

in Al_2O_3 content, the oxidizing property and dephosphorization capability of the slag were enhanced. Xu et al. [9] and Wang et al. [10] found that the mechanism by which Na_2O reduces slag viscosity is by increasing non-bridging and free oxygen in the slag and decreasing the number of $[\text{SiO}_4]^{4-}$ and $[\text{AlO}_4]^{4-}$ tetrahedra, thus reducing the network structure of the slag. Xie et al. [11] and Geng et al. [12] showed that Na_2O can replace CaO in the solid solution to form $2\text{CaO}\cdot\text{SiO}_2\text{-Na}_2\text{O}\cdot 2\text{CaO}\cdot\text{P}_2\text{O}_5$ solid solution, increasing the distribution ratio of P_2O_5 in the slag, and Li et al. [13] found that adding 0 to 1.75% Na_2O in MgO -saturated CaO-FeO-SiO_2 slag increased the phosphate capacity from $10^{18.37}$ to 10^{19} . Diao et al. [14] and Xuan et al. [15] showed that adding both Al_2O_3 and Na_2O to fluoride-free CaO-FeO-SiO_2 slag results in better dephosphorization than adding Al_2O_3 or Na_2O alone; with controlled $w(\text{Na}_2\text{O})$ at 0.7 to 3.1% and $w(\text{Al}_2\text{O}_3)$ at 2.5 to 7.9%, a dephosphorization rate of over 90% can be achieved. More importantly, both Al_2O_3 and Na_2O can enhance the enrichment of phosphorus in steel slag, with Al_2O_3 increasing P_2O_5 content in the $2\text{CaO}\cdot\text{SiO}_2\text{-3CaO}\cdot\text{P}_2\text{O}_5$ (C2S-C3P) phase [16,17], and Na_2O forming the high-phosphorus solid solution $\text{Na}_2\text{Ca}_4(\text{PO}_4)_2\text{SiO}_4$ [18], thereby facilitating the recovery and utilization of phosphorus in steel slag. The above thoroughly demonstrates that materials rich in Al_2O_3 and FeO , with a small amount of Na_2O , are ideal for preparing fluoride-free steelmaking fluxes.

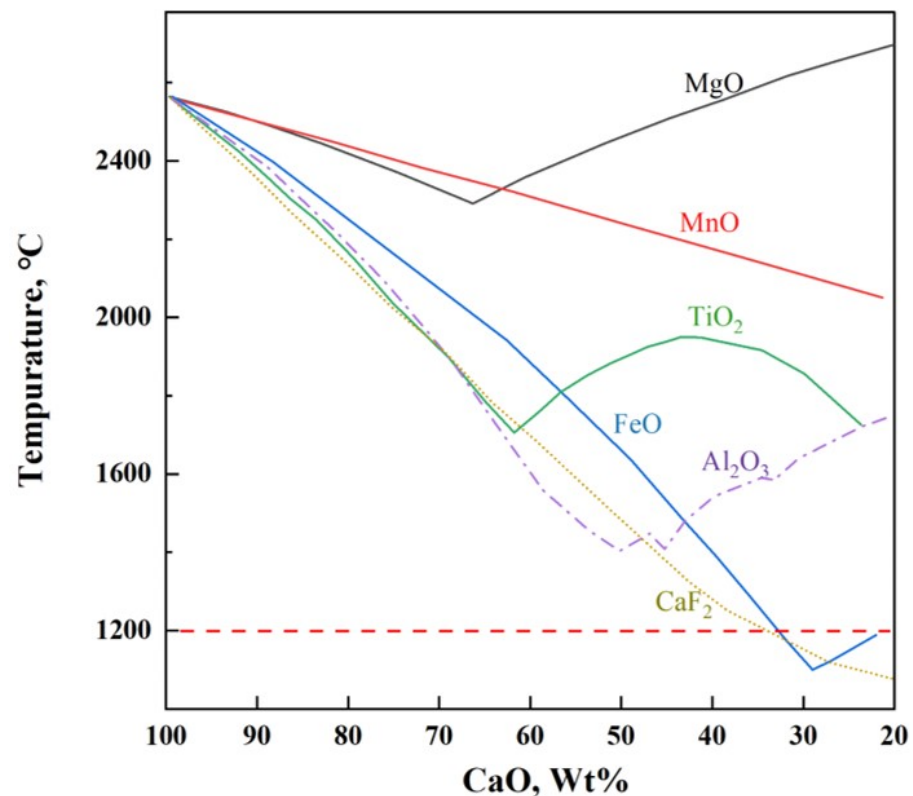


Figure 1. Melting points of CaO-based binary mixtures.

Red mud is a major solid waste generated in the process of alumina production. In China, the majority of alumina enterprises employ the Bayer process, resulting in red mud enriched with high contents of Fe_2O_3 and Al_2O_3 , accompanied by SiO_2 , Na_2O , TiO_2 , and CaO [19]. Yang et al. [20] utilized red mud in the hot metal pre-treatment dephosphorization process, showing that its addition effectively improved the fluidity of dephosphorization slag and enhanced the rate of pre-dephosphorization. Bang et al. [21] and Jeong et al. [22] showed that the preparation of desulfurization melts using red mud could achieve or outperform the desulfurization with the use of CaF_2 melts. Our team performed a systematic study on the feasibility of using Bayer red mud as a flux in steelmaking, finding that adding red mud to the CaO-FeO-SiO_2 slag system significantly expanded the liquid

phase region between 1300 °C and 1400 °C, extending towards higher CaO content and lower FeO content, indicating the possibility of achieving good fluidity under high alkalinity and low FeO content conditions [23]. Dephosphorization experiments in a 200 kg induction furnace [24] showed that using red mud as a flux, under semi-steel conditions ($[C] = 2.5\text{--}3.0\text{ wt\%}$), reduced the $[P]$ in the melt pool to below 0.02 wt% (initial $[P]$ in hot metal was 0.17 wt%), with a dephosphorization rate of over 90%, fully demonstrating the fluxing effect of red mud in deep dephosphorization. Results from dephosphorization experiments with medium-high phosphorus hot metal ($w[P] = 0.37\%$) [25] showed that when the red mud to lime ratio was 1:1.2, the final $[P]$ was 0.02 wt%, compared to 0.17 wt% without red mud under the same conditions; the $P_2O_5\%$ content in the dephosphorization slag with added red mud reached 15.49 wt%, which meets the national standard (GB/T20412-2021) [26] for calcium magnesium phosphate fertilizers. Without red mud, the $P_2O_5\%$ content in dephosphorization slag was up to 5.7 wt%, primarily due to the increased ability of components like Al_2O_3 and Na_2O to enhance the dissolution of P_2O_5 in the phosphorus-rich phase.

The research presented above demonstrates the potential of Bayer process red mud, rich in components such as Fe_2O_3 , Al_2O_3 , and Na_2O , to serve as a fluoride-free flux in the steelmaking process. However, due to its unique mineralogical structure, red mud has a high melting point (usually $>1350\text{ °C}$). This high melting point poses challenges in the early stages of basic oxygen steelmaking, especially before the intense carbon-oxygen reaction (when the melt pool temperature reaches 1420 °C), as it hinders rapid melting and limits the fluxing effect of components like Al_2O_3 [1,8]. Moreover, red mud has a high water content (about 20 wt%) and fine granularity (50–100 μm), requiring processing before transportation [19].

This study initially used Bayer red mud as the primary raw material to prepare a low-melting-point flux significantly below the temperature of molten iron. This flux, upon rapid melting in the early stages of steelmaking, effectively facilitated lime dissolution and rapidly formed a fluid initial slag, enabling deep dephosphorization in the early stages of converter steelmaking and enhancing efficiency. This paper explores the optimal composition and fluxing mechanisms of red mud-based (RM-based) fluxes, analyzing the relationship between the melting temperature of RM-based fluxes and the lime dissolution rate, and examines its impact on dephosphorization in the early stages of smelting. This provides crucial evidence for the development of RM-based fluoride-free steelmaking fluxes and offers a feasible pathway for the large-scale utilization of red mud.

2. Thermodynamic Analysis on Composition of RM-Based Flux

Red mud from the Bayer process in China typically contains Fe_2O_3 , Al_2O_3 , and SiO_2 as its main components, with respective contents of 30–40 wt%, 15–25 wt%, and 10–20 wt%. It also contains smaller amounts of TiO_2 (2–8 wt%), Na_2O (5–10 wt%), and CaO (5–10 wt%). Figure 2a indicates that Bayer process red mud with Fe_2O_3 - Al_2O_3 - SiO_2 as the main components has a high melting temperature, which is not conducive to rapid melting under hot metal conditions or during the initial stages of converter smelting. Considering the modification of red mud's composition to preserve its high oxidizing property and to increase its alkalinity, the incorporation of CaO is contemplated. As shown in Figure 2b, within the Fe_2O_3 - Al_2O_3 - SiO_2 -10% CaO system, the lowest liquidus temperature is below 1400 °C. In the Fe_2O_3 - Al_2O_3 - SiO_2 -30% CaO system in Figure 2c, the lowest liquidus temperature can be reduced to below 1300 °C. Given the high alkalinity of steelmaking slag, it is imperative that the flux also retains high alkalinity, and the iron oxide content should be as high as possible [5,6]. The optimal composition of the flux includes CaO at 20–30 wt%, Fe_2O_3 at 35–45 wt%, Al_2O_3 at 10–15 wt%, and SiO_2 at 10–15 wt%. Specifically, Figure 2d reveals that in the CaO - Fe_2O_3 binary system, characterized by calcium ferrate, the lowest melting point is 1216 °C, with $CaFe_2O_4$ as the mineral phase. Although calcium ferrate is an effective steelmaking flux, its high production cost limits its use by domestic steel companies [27]. When a certain amount of Al_2O_3 is present in the

CaFe_2O_4 phase, it forms a type of calcium ferrate phase containing Al_2O_3 , also known as $\text{Ca}(\text{Al}, \text{Fe})_2\text{O}_4$. The melting point of this mineral phase further decreases to 1142°C , as shown in Figure 2e. Consequently, by adhering to the principle of mineral phase design, managing the $\text{CaO}/(\text{Fe}_2\text{O}_3 + \text{Al}_2\text{O}_3)$ ratio in systems primarily composed of Fe_2O_3 - Al_2O_3 - CaO to control the formation of calcium aluminate ferrate phases, and integrating a small quantity of Na_2O into these phases, can also decrease the melting point. Accordingly, the design and validation of the melting characteristics of RM-based fluxes were carried out.

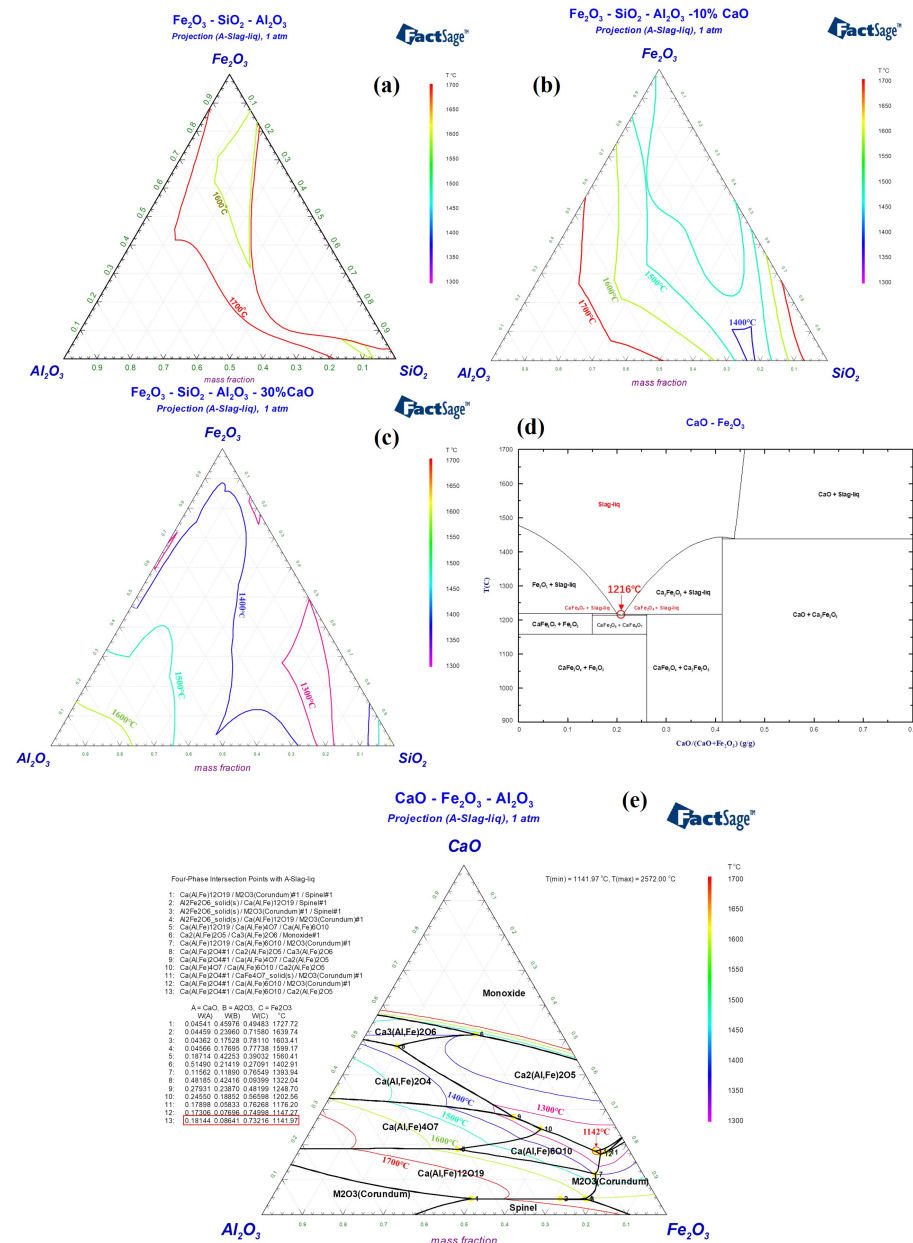


Figure 2. Liquid phase regions of (a) Fe_2O_3 - Al_2O_3 - SiO_2 , (b) Fe_2O_3 - Al_2O_3 - SiO_2 -10% CaO , (c) Fe_2O_3 - Al_2O_3 - SiO_2 -30% CaO , (d) CaO - Fe_2O_3 and (e) CaO - Fe_2O_3 - Al_2O_3 phase diagram.

3. Experimental

3.1. Materials

The two types of samples were taken in equally from four locations in the red mud dump (Jinxin Chemica, Baise, Guangxi, China), thoroughly mixed, and then set aside for further use, with about 100 g sampled each time. The composition of red mud is shown in Table 1. In the experiment, all samples were thoroughly dried at 105°C . The pig iron

utilized in the dephosphorization experiment was sourced from the Jinhui Steel company (Xuchang, Henan, China), with its particular composition detailed in Table 2. Based on the red mud composition presented in Table 1 and in conjunction with the phase diagram data in Figure 2, it is evident that to further decrease the melting point of the red mud flux, the addition of lime to the red mud is required, thereby shifting the composition towards the lowest melting point.

Table 1. Bayer red mud composition, wt%.

| Sample | Al ₂ O ₃ | SiO ₂ | Fe ₂ O ₃ | TiO ₂ | CaO | MgO | Na ₂ O | Bal. |
|-----------|--------------------------------|------------------|--------------------------------|------------------|-------|------|-------------------|------|
| Red mud A | 13.76 | 13.12 | 42.53 | 8.33 | 11.83 | 0.17 | 8.70 | 1.56 |
| Red mud B | 16.30 | 14.60 | 31.70 | 6.62 | 17.80 | 0.32 | 8.50 | 4.16 |

Table 2. Iron initial composition, wt%.

| C | Si | Mn | P | S |
|------|------|------|------|------|
| 4.30 | 0.40 | 0.32 | 0.16 | 0.04 |

3.2. Equipments

3.2.1. Measurement of Melting Temperature and Lime Dissolution Rate

The melting temperature of the RM-based flux and the lime dissolution rate can be evaluated using a high-temperature reaction in situ observation and online analysis system, as depicted in Figure 3a. The system comprises a three-dimensional super depth-of-field high-temperature video microscope (FLIR, FL3-U3, Portland, OR, USA), a high-temperature microscope equipped with contact angle measurement (Mirion, SEL100, Atlanta, Finland), and a high-temperature heating furnace (Yonekura, IR-QP, Niigata, Japan). The high-temperature heating furnace employs a halogen light source for heating, with a maximum temperature rise/fall rate of 1000 °C/min, and a temperature control precision of ±0.1 °C (B-Type Pt-30% Rh-Pt-6% Rh Thermocouple). It is outfitted with a HiTOS high-temperature observation system and a control processing system for real-time in situ observation, video image collection, and data recording. Temperature and time are also recorded in the real-time image obtained by the sensor. The melting temperature can be gauged using a horizontal side window position (Position 1), with the temperature regime as illustrated in Figure 3b. The lime dissolution rate can be determined using a vertical skylight position (Position 2), with the corresponding temperature regime as depicted in Figure 3c.

3.2.2. Experiment of Oxygen Blowing Steelmaking

The experiment, involving steelmaking dephosphorization under oxygen-blowing conditions, was conducted in a medium-frequency induction furnace with a capacity of 10 kg. The induction furnace, operating at a frequency of 4 kHz, has a power of 50 kW and can reach a maximum temperature of 1700 °C. The oxygen-blowing experiment entails the addition of an external oxygen-blowing device above the induction furnace to facilitate slag formation, dephosphorization, and decarburization, thereby simulating the converter steelmaking process.

3.3. Methods

3.3.1. Measurement of Melting Temperature

The experiment to determine the complete melting temperature of the samples was conducted as follows: red mud particles were ground to a size less than 80 µm. Different proportions of lime were then mixed evenly with the red mud. The mixture was molded into cylindrical shapes of 3 mm × 3 mm and placed on a square MgO base. This was then set on a corundum holder in the central heating area (∅15 mm × L50 mm) for high-temperature melting observation. As shown in Figure 4, the melting process of the RM-based flux included the following stages: shrinkage (Step 2), upper part melting into a spherical shape

(Step 3), and a decrease in height as the liquid phase increased. The temperature at the initial moment when the height of the test sample remained unchanged was recorded as the melting temperature of the slag (Step 4). The temperature at that moment could be read from the data recorded in the graph (white frame, accurate to 5 °C). Additionally, corresponding samples were taken for SEM-EDS (FEI, MLA250, Hillsboro, OR, USA) analysis to observe the microstructure and phase composition.

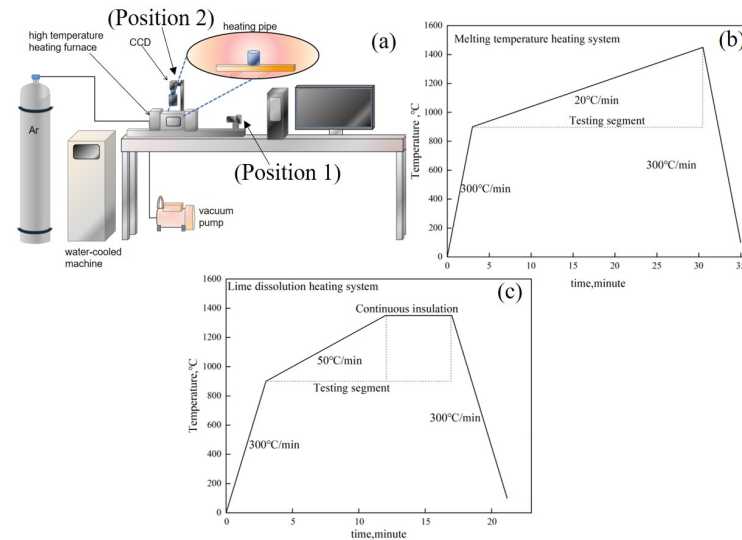


Figure 3. (a) High-temperature reaction in situ observation system, (b) heating regime for melting temperature tests, (c) heating regime for lime dissolution tests.

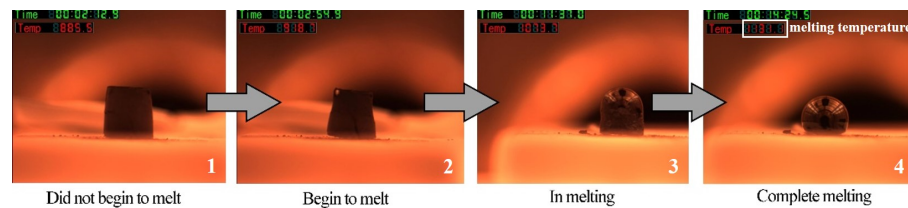


Figure 4. Melting temperature characterization.

As previously stated, to achieve the RM-based flux with the lowest melting point, a certain quantity of lime must be incorporated into both red mud A and B. In this study, red mud A and B were utilized as raw materials, with varying quantities of lime incorporated into each. The experimental plan was outlined in Table 3.

Table 3. Different proportions of flux preparation.

| Group | Red Mud | Quality of Red Mud (g) | Quality of Added CaO (g) |
|-------|-----------|------------------------|--------------------------|
| A1 | Red mud A | 100 | 0 |
| A2 | | 100 | 3 |
| A3 | | 100 | 10.6 |
| A4 | | 100 | 18 |
| A5 | | 100 | 28.5 |
| A6 | | 100 | 33 |
| B1 | Red mud B | 100 | 0 |
| B2 | | 100 | 2.3 |
| B3 | | 100 | 4.5 |
| B4 | | 100 | 8.9 |
| B5 | | 100 | 18.4 |
| B6 | | 100 | 22.3 |

3.3.2. Measurement of Lime Dissolution Rate

After preparing the flux from red mud and CaO, a 0.2 g (accurate to 0.001 g) mm initial sample was placed in a high-purity MgO crucible. Preliminary experiments indicated that 0.04 (accurate to 0.001 g) of lime was near the dissolution limit of the flux. During the experiment, lime pillars weighing 0.012 g, 0.024 g, and 0.04 g were placed on the flux samples, as shown in Figure 5, and the time required to completely dissolve the lime was recorded. The high-purity MgO crucible was placed on a MgO pad in the central heating area ($\varnothing 15 \text{ mm} \times L50 \text{ mm}$), and argon gas was introduced during the test for protection. Due to the small size and rapid dissolution of the lime pillars in this experimental method, it was difficult to use conventional methods of measuring diameter to obtain the lime dissolution rate. Instead, the complete dissolution time of lime pillars of different masses was determined using a super-depth-of-field microscope. The complete dissolution time started from the moment the lime began to dissolve until no solid phase was present in the entire field of view. It is noteworthy that after removing the aforementioned samples without any solid phase, tests on multiple groups of samples showed that the content of free calcium oxide was below the detection limit, indicating that the lime had completely dissolved in the slag. The formula for calculating the lime dissolution rate is

$$v_f = \frac{\Delta m_1}{\Delta t_1} \quad (1)$$

$$v_a = \frac{\Delta m_2}{\Delta t_2} \quad (2)$$

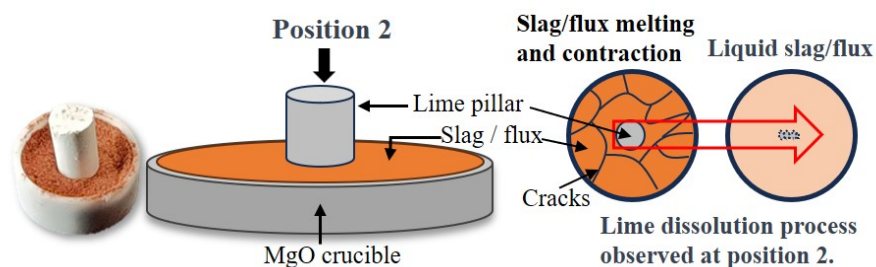


Figure 5. Lime dissolution rate test method.

In the formula, v_f is defined as the dissolution rate of 0.012 g of lime, g/s; Δm_1 is the mass of lime dissolved (0.012 g), g; Δt_1 is the time taken to dissolve 0.012 g of lime, s. v_a is defined as the average dissolution rate during the dissolution of 0.024 g or 0.04 g of lime, g/s; Δm_2 is the mass of the maximum lime dissolved (0.024 g or 0.04 g), g; Δt_2 is the total time required to dissolve 0.024 g or 0.04 g of lime, s.

3.3.3. Experiment of Oxygen Blowing Steelmaking

To compare the application effects of RM-based fluxes and CaF_2 in steelmaking, this study contrasted the dephosphorization effects under three conditions: adding only lime to the slag (NO.1), adding lime and CaF_2 flux (NO.2), and adding lime and RM-based flux A4 (NO.3), as outlined in Table 4. It is important to note that the amount of lime added was to ensure consistent final slag alkalinity, and the quantity of final slag under the same blowing conditions was similar. During the experiment, 3 kg of pig iron was heated in a magnesia crucible from room temperature to 1350 °C and maintained at this temperature for 5 min before taking the initial sample 1. Under the three experimental conditions, CaO, (CaO + CaF_2), and (RM-based flux + CaO) were, respectively, added to the molten iron surface and reacted for 5 min, after which steel and slag sample 2 were taken. Oxygen blowing then commenced, and after 4 min, steel and slag sample 3 was collected. The blowing continued for another 6 min before taking the final steel and slag sample 4 and tapping at high temperature. After the experiment, the crucibles containing

the quenched samples were placed in an oven to completely dry. The slag and pig iron were physically separated. Taking a 1 g pig iron sample and using a carbon/sulfur analyzer (CS, Eltra, CS-800, Haan, Germany) to check the [C] content, a 0.1 g sample was fully dissolved in a solution of 3 mol/L HCl and 1 mol/L HNO₃, and the [P] content was then determined using an inductively coupled plasma atomic emission spectrometer (ICP-MS, Thermo Scientific, ICAP RQ, Waltham, MA, USA).

Table 4. Experiments on dephosphorization of different melting flux.

| No. | Slag Material | | %CaO/%SiO ₂ | Slag Ratio | T/°C | Continuous Oxygen Blowing/min |
|-----|---------------|----------------------|------------------------|------------|------|-------------------------------|
| | CaO | Flux | | | | |
| 1 | 27 g | - | 3 | 2–3% | 1350 | 4 + 6 |
| 2 | 27 g | 5 g CaF ₂ | 3 | 2–3% | 1350 | 4 + 6 |
| 3 | 30.2 g | 35.4 g A4 | 3 | 2–3% | 1350 | 4 + 6 |

4. Results and Discussion

4.1. Melting Temperature of RM-Based Flux

The melting temperature results of RM-based fluxes are shown in Figure 6. The original red muds A and B had melting temperatures of 1360 °C (A1) and 1274 °C (B1), respectively. Overall, the melting temperatures of red mud fluxes formed by adding lime to both types of red mud displayed an initial increase followed by a decrease with the addition of CaO. The lowest melting temperatures for the A and B series of RM-based fluxes were 1161 °C (A4) and 1230 °C (B4), respectively. This indicated that during the melting process, CaO reacted with components present in red mud, such as Fe₂O₃ and Al₂O₃, to form a sufficient quantity of low-melting-point phases, such as CaFe₂O₄ and Ca(Fe,Al)₂O₄, thereby reducing the overall melting temperature of the slag [28]. The CaF₂-CaO phase diagram indicates that their lowest eutectic temperature is 1360 °C [7]. However, Figure 7 demonstrates that the appropriate composition of RM-based fluxes can reduce the melting temperature of lime to below 1200 °C, thereby more effectively facilitating lime dissolution.

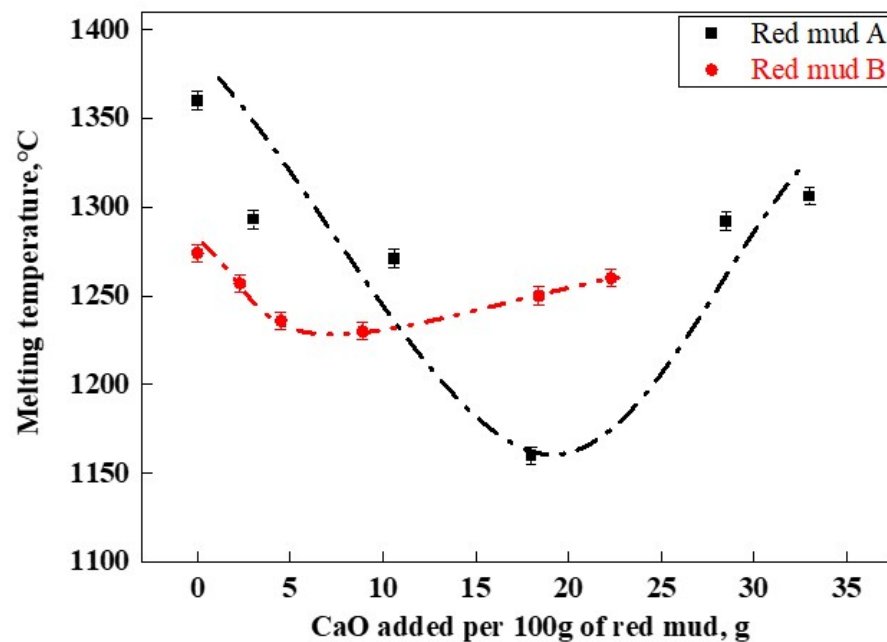


Figure 6. RM-based flux melting temperature.

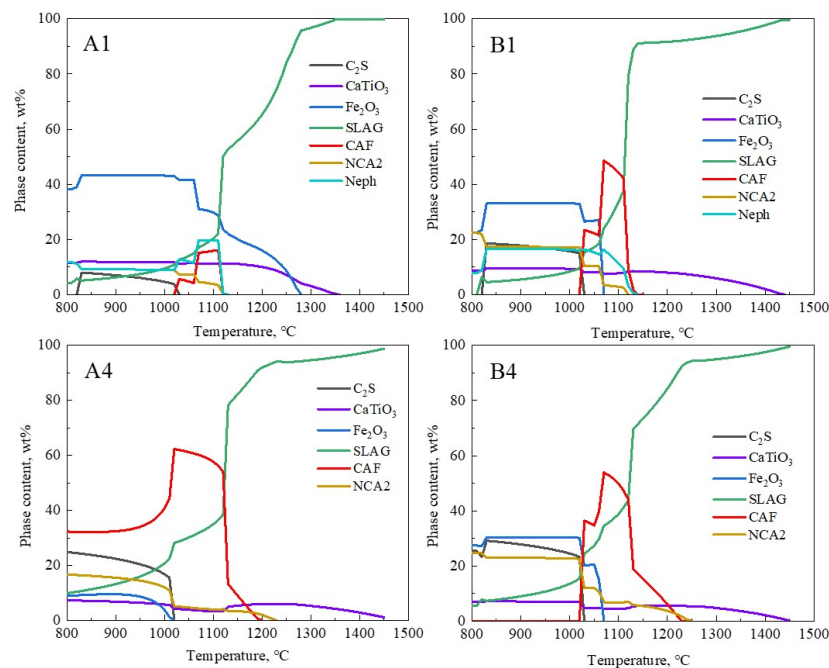


Figure 7. Effect of temperature on mineral phases in different fluxes.

4.2. Melting Mechanism of RM-Based Flux

The overall melting temperature of the flux decreased, closely linked to the formation of low-melting-point phases. The thermodynamic software FactSage 8.1 (GTT Technologies, Aachen, Germany and Thermfact/CRCT, Montreal, QC, Canada) was used to predict the phase evolution of the samples [29]. For the calculations, the equilibrium module was employed together with the databases FToxid. The phase evolution process of the original red mud samples (A1 and B1) and the samples with the lowest melting temperatures (A4 and B4) at different temperatures is shown in Figure 7. The CAF phase represents the calcium ferrate phase containing Al_2O_3 , also known as the calcium aluminoferrate phase ($\text{Ca}(\text{Fe},\text{Al})_2\text{O}_4$); NCA2 represents the Na-containing low-melting-point phase ($\text{Na}_2\text{CaAl}_4\text{O}_8$); Neph represents the nepheline phase ($\text{Na}(\text{Fe},\text{Al})\text{SiO}_4$); C_2S represents the calcium silicate phase (Ca_2SiO_4); SLAG represents the liquid slag. Figure 7 shows that for groups A4 and B4, within the 800 °C to 960 °C range, the SLAG phase is primarily composed of the Na-containing low-melting-point phase. As the content of NCA2, C_2S , and Fe_2O_3 gradually decreases, the corresponding SLAG phase increases, and around 960 °C, the CAF phase begins to form in large quantities. In the range of 960 °C to 1160 °C, the reaction of C_2S with Fe_2O_3 is complete, and the amount of CAF phase reaches its maximum, corresponding to the rapid melting stage of the slag. The CAF phases in groups A4 and B4 completely melted at 1190 °C and 1220 °C, respectively, and this corresponded to over 90% of the SLAG phase. This temperature range essentially matched the actual melting temperatures of A4 and B4 samples shown in Figure 6, indicating that the formation and melting of CAF phases significantly determined the overall complete melting temperature of the slag. Comparing groups A and B, the addition of CaO to the RM-based fluxes noticeably increased the formation of low-melting-point CAF phases, thereby lowering the flux's melting temperature. In group A4, the calculated content of CAF phases in the flux reached 60%, corresponding to the lowest melting temperature in that system. Thus, there is an intrinsic connection between the complete melting temperature of RM-based fluxes and the formation and melting of low-melting-point CAF phases in the slag system.

To validate the relationship between the formation of low-melting-point phases and the melting temperature of fluxes, SEM-EDS analysis was conducted on the original red mud groups (A1, B1) and the RM-based fluxes with the lowest melting temperatures (A4, B4).

Figure 8a and Table 5 present the mineralogical morphology and corresponding composition of the four flux groups after rapid cooling at 1000 °C. The results showed that the mineral compositions of the original red mud fluxes A1 and B1 were identical, including Hercynite (Fe_3O_4 , $(\text{Fe}, \text{Ca})\text{Al}_2\text{O}_4$), Perovskite (CaTiO_3), NCA2, and Nepheline, with no observed CAF phases. This was consistent with the thermodynamic predictions for A1 and B1 in Figure 7, indicating the presence of high-melting-point Fe_2O_3 and a small amount of CaTiO_3 between 1400 °C to 1000 °C. The mineral compositions of the RM-based fluxes A4 and B4 were also the same, including Hercynite, CAF phases, Perovskite, and NCA2. This was in line with the thermodynamic predictions for A4 and B4 in Figure 7, where CaTiO_3 , iron spinel phase (Fe_2O_3), and a significant amount of CAF phases were present during the cooling process from 1400 °C to 1000 °C.

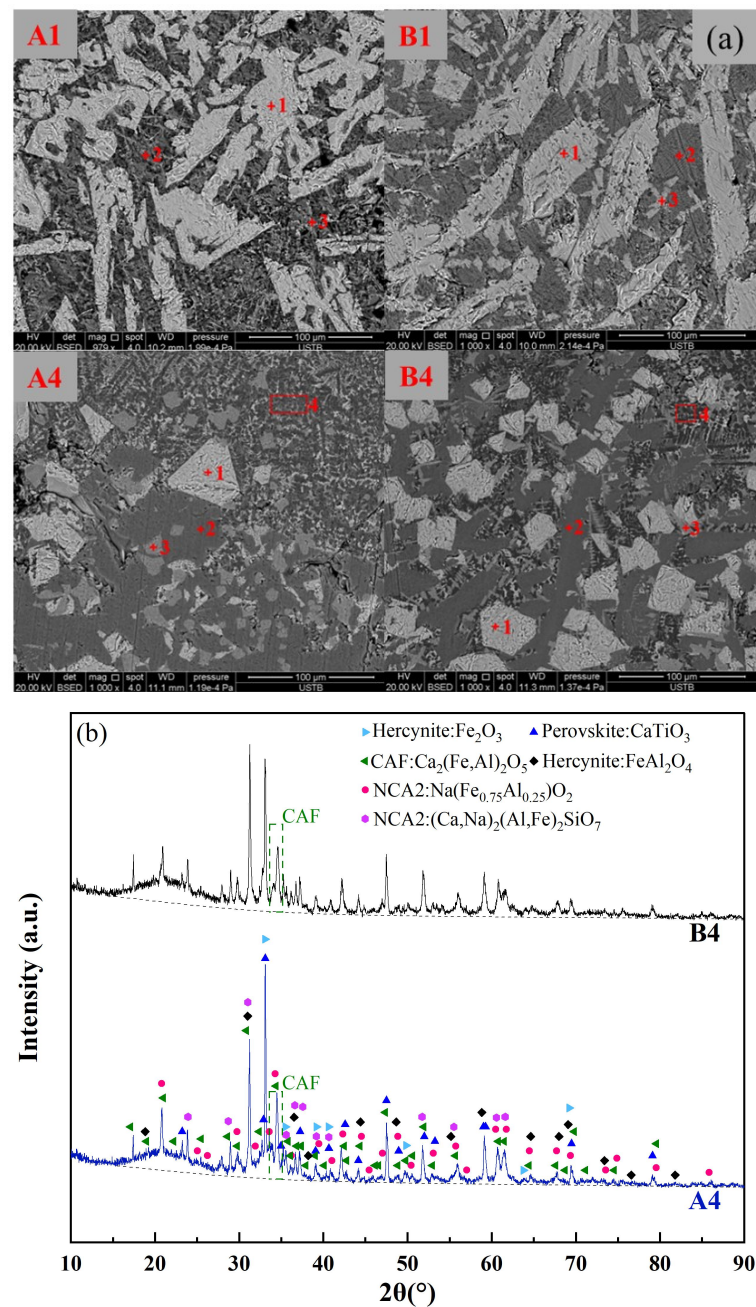


Figure 8. (a) Mineral phase morphology of red mud slag rapidly cooled at 1000 °C, (b) XRD pattern of A4 and B4 rapidly cooled at 1000 °C.

Table 5. EDS energy spectrum analysis.

| No | Point | Element Content (Atom, wt%) | | | | | | | Phase |
|----|-------|-----------------------------|-------|-------|-------|------|-------|-------|--------------------|
| | | O | Fe | Al | Ca | Si | Na | Ti | |
| A1 | 1 | 50.57 | 43.38 | 4.03 | | | | 2.01 | Hercynite |
| | 2 | 50.67 | 4.45 | 11.95 | 17.67 | 9.93 | 5.33 | | Slag1 |
| | 3 | 54.79 | 4.94 | | 21.66 | 1.98 | | 16.63 | CaTiO ₃ |
| B1 | 1 | 47.77 | 27.98 | 15.47 | 8.77 | | | | Hercynite |
| | 2 | 52.29 | 4.96 | 10.64 | 11.94 | 8.75 | 7.92 | 3.5 | Slag |
| | 3 | 52.87 | 6.00 | | 23.42 | | | 17.70 | CaTiO ₃ |
| A4 | 1 | 40.44 | 52.87 | 6.69 | | | | | Hercynite |
| | 2 | 46.26 | 4.34 | 18.40 | 22.43 | 8.58 | | | CAF |
| | 3 | 50.88 | 9.66 | 3.42 | 22.60 | 2.51 | | 10.92 | CaTiO ₃ |
| | 4 | 44.49 | 11.97 | 11.96 | 11.71 | 5.51 | 12.59 | 1.78 | NCA2 |
| B4 | 1 | 32.22 | 60.27 | 6.61 | 0.89 | | | | Hercynite |
| | 2 | 42.43 | 4.71 | 18.29 | 24.77 | 9.80 | | | CAF |
| | 3 | 48.07 | 7.11 | 1.68 | 24.68 | 1.62 | | 16.85 | CaTiO ₃ |
| | 4 | 42.23 | 13.25 | 13.26 | 10.97 | 5.55 | 13.59 | 1.15 | NCA2 |

The XRD analysis was carried out for both A4 and B4 melts, as shown in Figure 8b. The presence of the CAF phase, Hercynite, Perovskite, and NCA2 was confirmed for both groups of CaO-added melts. Comparing the intensity of the primary peak position represented by the CAF phase, it was observed that the content of the CAF phase in A4 was higher than that in B4. Furthermore, a certain amount of amorphous phase (i.e., liquid slag) was identified in both A4 and B4, with the content of the liquid slag phase in A4 being higher than that in B4. These liquid slag phases exhibit significantly lower melting points (below 1000 °C), thereby facilitating a reduction in the overall melting temperature of the melt. Based on the SEM-EDS results, it was observed that the microscopic morphology and composition of the liquid slag phases and CAF phases were largely consistent. This phenomenon could be attributed to the rapid cooling of the sample, leading to high supercooling conditions, wherein these phases were not completely precipitated. In conclusion, the formation of the CAF phase and other low-melting-point phases in the RM-based flux contributed to a decrease in the overall melting temperature compared to the pristine red mud.

After exporting the data from the thermodynamic calculations mentioned above, the maximum mass fractions of the CAF phase were analyzed and summarized for the same temperature intervals for groups A and B. The correlation between the maximum mass fractions of CAF phases produced by each flux composition and the measured melting temperatures of these fluxes was depicted in Figure 9. The results indicated that higher mass fractions of CAF phases corresponded to lower melting temperatures. For instance, group A4, with 64% CAF phase content, exhibited the lowest complete melting temperature of 1161 °C; group B4, with 42% CAF phase content, had the lowest complete melting temperature of 1230 °C. These findings were consistent with the main conclusions displayed in Figures 7 and 8, indicating that the amount of CAF phase produced significantly determined the complete melting temperature of the flux and was the primary phase affecting flux melting. For the same red mud, the addition of CaO mainly influenced the formation of CAF phases; the more CAF phases generated, the lower the melting point of the flux.

4.3. Lime Dissolution Rate of RM-Based Flux

Figure 10a depicts the lime dissolution rates in different fluxes, where groups A1–A5 represent RM-based fluxes prepared by mixing red mud A with various amounts of lime (Table 3). Group 0 served as a control experiment, utilizing a pure chemical reagent mixture with a composition of 37.5% CaO, 37.5% SiO₂, 20% Fe₂O₃, and 5% MgO. This mixture was pre-melted at 1500 °C and then formed into test samples to analyze and test the lime dissolution rate under basic oxygen steelmaking slag conditions at the beginning of the process (R = 1, without other fluxes). It was evident that under RM-based flux conditions,

the lime dissolution rates were higher than those at the beginning of the basic oxygen steelmaking process (group 0). The fastest dissolution rates occurred during the initial phase of dissolving 0.012 g of lime. Group A4, the fastest, dissolved 0.012 g of lime in only 42 s, while the slowest, group A1 with added RM-based flux, took 6 min and 48 s. The control group 0, without any flux, took 7 min and 54 s. Groups 0 and A5 were unable to completely dissolve 0.04 g of lime under their experimental conditions, whereas the RM-based fluxes A1–A4 succeeded in fully dissolving 0.04 g of lime. The dissolution time for A4 was the fastest at 3 min and 55 s, and group A1, which was pure red mud flux (without added CaO, as shown in Table 3), took 23 min. The discussion in this work regarding the dissolution rate of lime in the flux does not necessitate a detailed consideration of the dissolution behavior of the flux itself. However, this aspect presents an intriguing topic for future research.

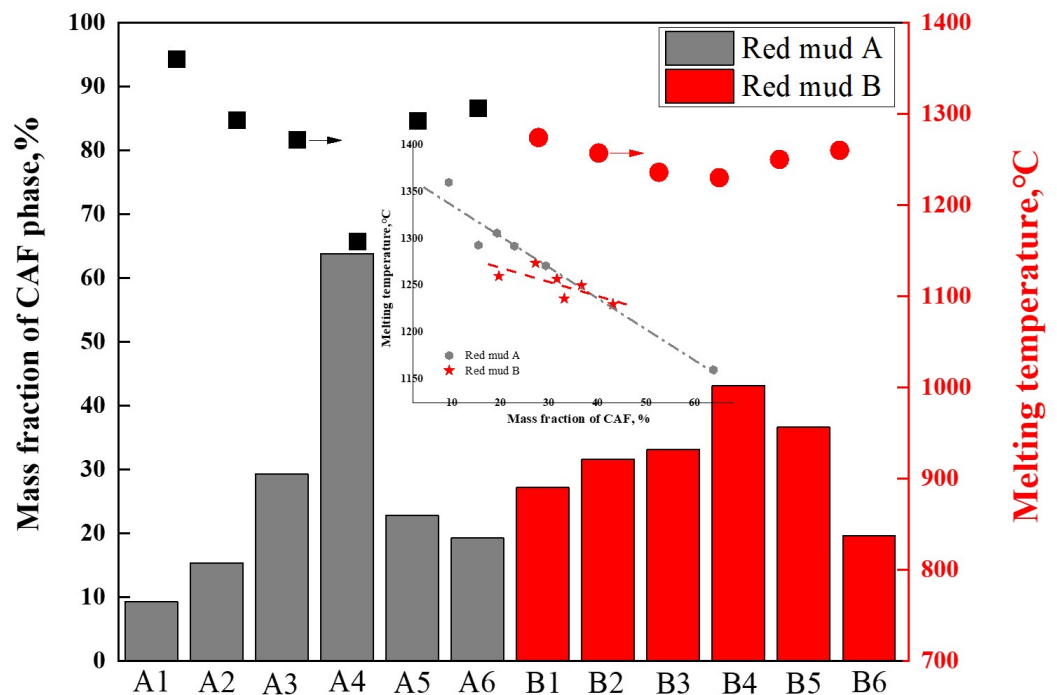


Figure 9. Effect of CAF phase content on melting temperature

As shown in Figure 10b, the fastest and average dissolution rates (v_f and v_a , respectively) of different fluxes were calculated. The fastest dissolution rate indicates the efficiency of the flux on the melting of lime, which affects the speed of lime melting in the early stage of steelmaking. The average dissolution rate represents the utilization rate of the flux on lime, which influences the f-CaO of the final slag in steelmaking. The A4 and A3 groups demonstrate significant advantages in both the fastest and average dissolution rates. Compared with the steelmaking slag without flux, the lime dissolution rate of the optimal A4 group increased by about 12 times. Even in the A5 sample with high lime content, the dissolution rate is slightly faster than the lime dissolution rate of pure red mud, which proves that the flux has a higher dissolution amount of lime. Additionally, combining the melting temperature data with the lime dissolution rate data, it can be clearly observed that the lower the melting point of the RM-based flux, the higher its dissolution rate of lime. group A1, with the highest melting temperature, showed the lowest dissolution rate, while group A4, with the lowest melting temperature, exhibited the highest rate. This can be attributed to two factors. On the one hand, the lower melting temperature, correlated with a higher content of low-melting-point phases, allows for the rapid formation of more of the liquid phase, increasing the contact area of lime particles [30]. On the other hand, the formation of CaO-containing phases in the flux, as indicated by the phase evolution, further enhances the lime's dissolution capability. However, the study of Vieira et al. [31]

indicated that the dissolution rate of CaO decreased with increasing FeO/SiO₂ ratio, while Hamano et al. [32] found that the dissolution rate of CaO increased with increasing FeO content. These findings suggested that the present study deviated from the theories proposed in both of the aforementioned studies. Notably, the saturated solubility of CaO had been repeatedly discussed in the literature [30], with the formation of the 2CaO·SiO₂ phase identified as a direct contributor to saturation solubility in these investigations. It could be inferred that the emergence of new CaO-containing phases (e.g., the CAF phase) played a significant role in enhancing saturation solubility. Consequently, the current study aligned with existing theory while also broadening its applicability.

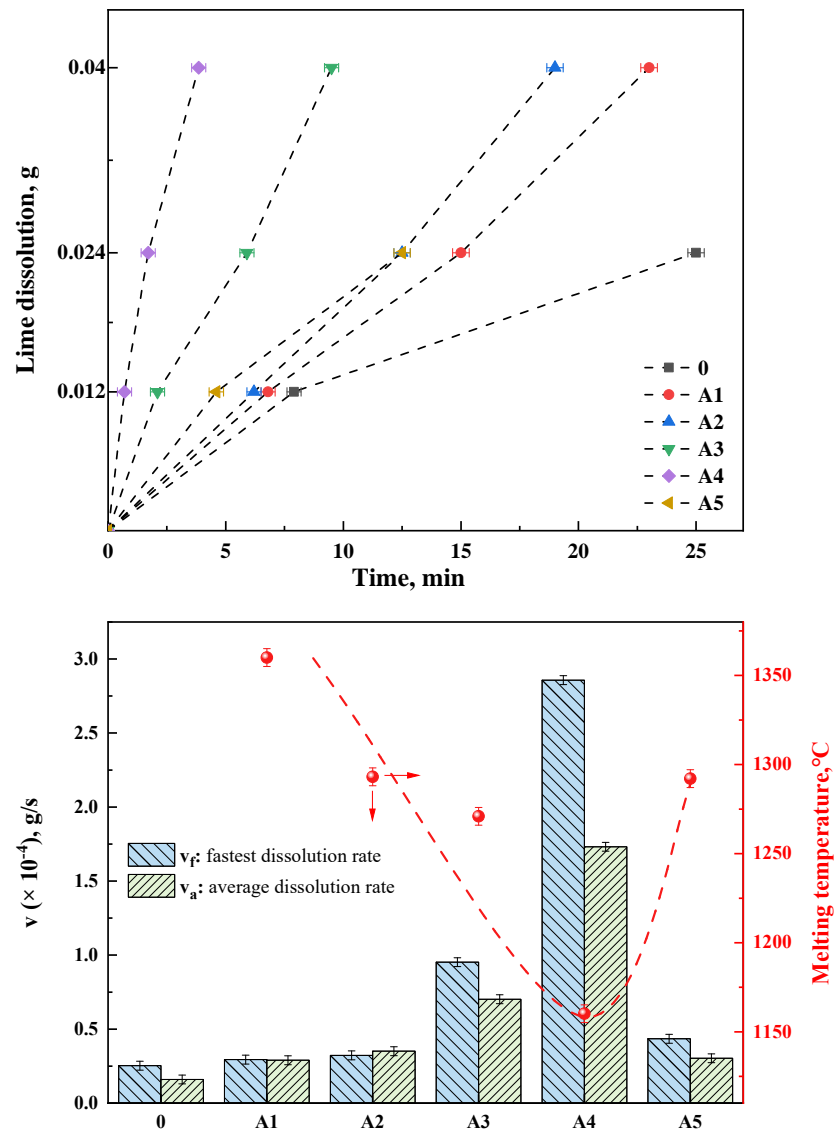


Figure 10. (top) Lime dissolution time of different fluxes, (bottom) Lime dissolution rate and melting temperature of RM-based flux in group A.

This leads to the fundamental principles for RM-based fluoride-free fluxes: lime-added RM-based fluxes are superior to red mud used directly as a flux. The optimal RM-based flux should possess a melting temperature below 1200 °C, with as high iron oxide and calcium oxide content as possible. The controlling strategy involves maximizing the content of low-melting-point CAF phases in the flux.

4.4. Application of Flux in Dephosphorization in 10 kg Induction Furnace

The flux A4, which exhibited the lowest melting point, was developed in the aforementioned study. To ascertain its metallurgical capabilities in facilitating slag formation and dephosphorization, steelmaking experiments were conducted in a 10 kg induction furnace. The variations in [C] and [P] content over time in the molten metal under three different slag formation methods were shown in Figure 11. It was observed that all three slag formation methods demonstrated dephosphorization capabilities. However, the addition of RM-based flux A4 significantly enhanced the dephosphorization effect, surpassing that of the CaF₂ flux (group NO.2) and the group without any flux (NO.1), particularly under non-oxygen-blowing hot metal conditions. Within the first 5 min before oxygen blowing, the addition of lime and RM-based flux reduced the [P] content from 0.16 wt% to 0.10 wt%, achieving a dephosphorization rate of 38%. In contrast, groups NO.1 (CaO addition) and NO.2 (CaO + CaF₂ addition) showed negligible dephosphorization during the same period. Within 4 min of oxygen blowing, group NO.1 without any flux showed limited dephosphorization efficiency, with [P] content reducing from 0.16 wt% to 0.127 wt% (a dephosphorization rate of only 20.6%). In contrast, group NO.2 with CaF₂ experienced a rapid decrease in [P] content to 0.055 wt% (dephosphorization rate of approximately 65.6%). Similarly, group NO.3 with the RM-based flux also reduced [P] to 0.055 wt%, mirroring the effect of CaF₂ addition. At this point, the [C] content in the hot metal was approximately 3.6%, indicating that both RM-based flux and CaF₂ can assist in achieving high dephosphorization rates at high [C] content. Continuing oxygen blowing for an additional 10 min, groups NO.1-NO.3 showed [P] contents of 0.072 wt%, 0.036 wt%, and 0.031 wt%, with dephosphorization rates of 55%, 77.5%, and 80.6%, respectively. Post-experiment, the [C] contents were 1.5 wt%, 1.8 wt%, and 2.2 wt% for the three groups. It is evident that under oxygen-blowing conditions, the RM-based flux A4 exhibited dephosphorization and fluxing effects comparable to CaF₂. However, in the pre-treatment of hot metal without oxygen blowing, its performance in both aspects was superior. Thus, the low-melting-point RM-based flux has the potential to replace CaF₂, making it an excellent fluoride-free flux option.

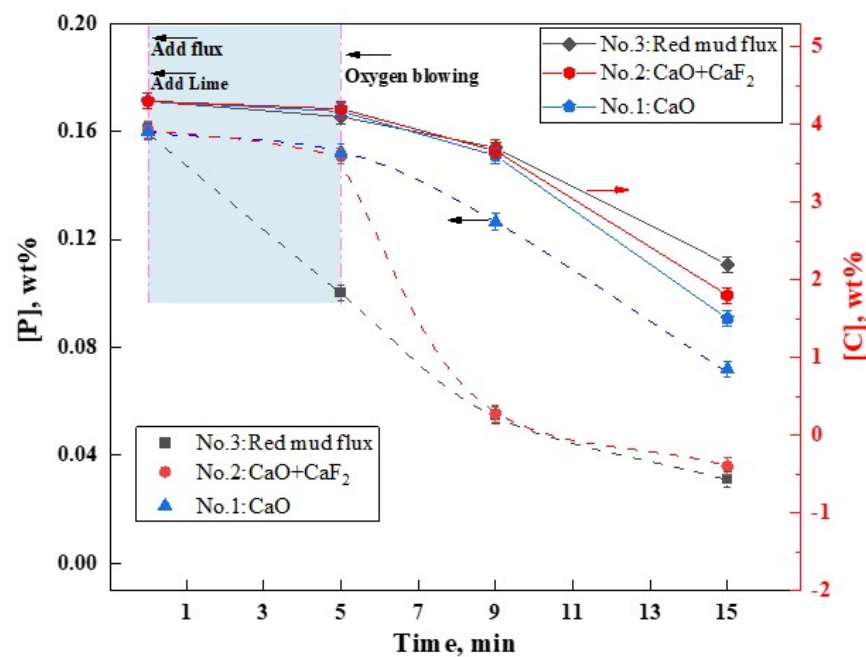


Figure 11. Effect of RM-based flux on dephosphorization.

5. Conclusions

This study utilized Bayer process red mud as the main raw material to develop a low-melting-point steelmaking flux. The melting point and lime dissolution rate of the RM-based flux were evaluated using a high-temperature in situ analysis system. A comparative study was performed in a 10 kg induction furnace to examine the effects of RM-based flux and CaF₂ on steelmaking dephosphorization, assessing the feasibility of using RM-based flux as a fluoride-free steelmaking flux. The specific conclusions were as follows:

1. The addition of lime to Bayer red mud showed a trend of initially decreasing and then increasing melting points. This is primarily due to the formation of low-melting-point CAF phases during the melting process. The more CAF phases formed, the lower the melting point. When lime was added to the red mud A, as indicated in the text, to prepare RM-based flux, the melting point reached a minimum of 1161 °C. This flux rapidly melts under steelmaking conditions, with components like Al₂O₃, Na₂O, and Fe₂O₃ in the red mud effectively reducing the lime's melting point. This facilitates the formation of a fluid initial slag, showing promise for use as a fluoride-free flux in steelmaking.
2. The dissolution rates of lime in various RM-based fluxes were analyzed. The results indicated that the lower the melting temperature in RM-based flux, the higher the corresponding lime dissolution rate. Notably, flux A4, with the lowest melting point of 1161 °C, exhibited an average lime dissolution rate of 1.73×10^{-4} g/s, which is 10 to 15 times that of the early basic oxygen steelmaking slag systems (with R about 1).
3. Experiments in a 10 kg induction furnace demonstrated that the addition of RM-based fluxes resulted in a pre-dephosphorization rate of nearly 40% under hot metal conditions without oxygen blowing, surpassing the performance of CaF₂ fluxes in the absence of oxidizers like Fe₂O₃. The primary reason for this enhanced performance is the high Fe₂O₃ content and low melting point in RM-based fluxes, which provide favorable thermodynamic and kinetic conditions for hot metal dephosphorization. Under oxygen-blowing conditions, the dephosphorization rate with RM-based fluxes was comparable to that of CaF₂, significantly higher than scenarios without any flux, especially at high [C] content. The data suggest that RM-based fluxes are highly suitable as fluoride-free alternatives in the steelmaking process, with considerable potential for widespread application.

Author Contributions: Conceptualization, Z.Z. and Y.Z.; methodology, K.Y.; software, Z.Z.; validation, Z.Z. and K.Y.; formal analysis, K.Y.; investigation, Z.Z.; resources, Z.Z.; data curation, Z.Z. and K.Y.; writing—original draft preparation, Z.Z.; writing—review and editing, Z.Z. and Y.Z.; visualization, Z.Z.; supervision, Y.Z.; project administration, Y.Z.; funding acquisition, Y.Z. All authors have read and agreed to the published version of the manuscript.

Funding: This work was supported by the National Key R&D Program of China (2019YFC1905701), the National Natural Science Foundation of China (U1960201).

Data Availability Statement: The raw data supporting the conclusions of this article will be made available by the authors on request.

Conflicts of Interest: The authors declare no conflicts of interest.

References

1. Elizaveta, C.; Stefanie, L.; Johannes, R.; Johannes, S.; Felix, F.; William, J.; Thierry, C.; Michael, N. Assessment of the dissolution rate and behaviour of raw dolomite and limestone with different calcination degrees in primary steelmaking slags. *Ironmak. Steelmak.* **2023**, *50*, 379–391. [[CrossRef](#)]
2. Wang, H.M.; Yang, L.L.; Li, G.R.; Zhu, X.; Zhu, H.; Zhao, Y.T. Effects of B₂O₃ and CaF₂ on Melting Temperatures of CaO-SiO₂-Fe₂O₃ System Fluxes. *J. Iron Steel Res. Int.* **2013**, *20*, 21–24. [[CrossRef](#)]
3. Fox, A.B.; Mills, K.C.; Lever, D.; Bezerra, C.; Valadares, C.; Unamuno, I.; Laraudogoitia, J.J.; Gisby, J. Development of Fluoride-Free Fluxes for Billet Casting. *ISIJ Int.* **2005**, *45*, 1051–1058. [[CrossRef](#)]
4. Prakash, G.; Sujeet, K.; Jallu Hari, B.; Gopal Shantaram, M.; Tapas Kumar, R. Production of low phosphorous steel from low silicon high phosphorous hot metal in BOF. *Ironmak. Steelmak.* **2023**, *50*, 1014–1021. [[CrossRef](#)]

5. Deng, T.; Gran, J.; Sichen, D. Dissolution of Lime in Synthetic 'FeO'-SiO₂ and CaO-'FeO'-SiO₂ Slags. *Steel Res. Int.* **2010**, *81*, 347–355. [[CrossRef](#)]
6. Ban-Ya, S.; Hino, M.; Nagabayashi, R.; Terayama, O. Dephosphorization and Desulphurization of Hot Metal with CaO-Al₂O₃-Fe_xO_y Flux. *Tetsu-to-Hagané* **1989**, *75*, 66–73. [[CrossRef](#)] [[PubMed](#)]
7. Ishikawa, M.; Matsuo, T.; Kawaguchi, T. Hot Metal Dephosphorization Behavior by Sintered Dephosphorization Agent Contain Al₂O₃. *Tetsu-to-Hagané* **2005**, *91*, 528–536. [[CrossRef](#)]
8. Li, J.; Wang, S.J.; Xia, Y.J.; Kong, H. Study on Dephosphorisation of Hot Metal Pretreatment with Al₂O₃ to Replace CaF₂ in Slag. *Ironmak. Steelmak.* **2014**, *42*, 70–73. [[CrossRef](#)]
9. Xu, R.Z.; Zhang, J.L.; Han, W.X.; Chang, Z.Y.; Jiao, K.X. Effect of BaO and Na₂O on the Viscosity and Structure of Blast Furnace Slag. *Ironmak. Steelmak.* **2018**, *47*, 168–172. [[CrossRef](#)]
10. Wang, L.; Zhang, C.; Cai, D.; Zhang, J.; Sasaki, Y.; Ostrovski, O. Effects of CaO/SiO₂ Ratio and Na₂O Content on Melting Properties and Viscosity of SiO₂-CaO-Al₂O₃-B₂O₃-Na₂O Mold Fluxes. *Metall. Mater. Trans. B* **2017**, *48*, 516–526. [[CrossRef](#)]
11. Xie, S.; Wang, W.; Liu, Y.; Matsuura, H. Effect of Na₂O and B₂O₃ on the Distribution of P₂O₅ between Solid Solution and Liquid Phases Slag. *ISIJ Int.* **2014**, *54*, 766–773. [[CrossRef](#)]
12. Geng, B.; Zhan, D.; Jiang, Z.; Yang, Y. Effect of CaO-MgO-FeO-SiO₂-x Na₂O Slag System on Converter Dephosphorization. *Metals* **2023**, *13*, 844. [[CrossRef](#)]
13. Li, G.; Hamano, T.; Tsukihashi, F. The Effect of Na₂O and Al₂O₃ on Dephosphorization of Molten Steel by High Basicity MgO Saturated CaO-FeOx-SiO₂ Slag. *ISIJ Int.* **2005**, *45*, 12–18. [[CrossRef](#)]
14. Diao, J. Effect of Al₂O₃ and Na₂O on Dephosphorization of High Phosphorus Hot Metal. *J. Iron Steel Res.* **2013**, *25*, 9–12.
15. Xuan, X.Y.; Shi, Z.; Qi, X.; Cai, J.W. Study on Dephosphorization of High-Phosphorus Hot Metal in CaO-SiO₂-FeO-Na₂O-Al₂O₃ Slag System. *Min. Metall* **2015**, *24*, 51–54.
16. Xie, S.; Wang, W.; Pan, Z.; Li, H.; Huang, D.; Du, Y. Effect of Al₂O₃ on the Melting, Viscosity, and Phosphorus Distribution of CaO-SiO₂-Fe₂O₃-P₂O₅ Slag System. *Steel Res. Int.* **2018**, *89*, 1700516. [[CrossRef](#)]
17. Jiang, L.; Diao, J.; Yan, X.; Xie, B.; Ren, Y.; Zhang, T.; Fan, G. Effect of Al₂O₃ on Enrichment of Phosphorus in Hot Metal Dephosphorization Slag. *ISIJ Int.* **2015**, *55*, 564–569. [[CrossRef](#)]
18. Lin, L.; Bao, Y.P.; Jiang, W.; Wu, Q.F. Effect of Na₂O on Phosphorus Enrichment and Separation in P-bearing Steelmaking Slag. *ISIJ Int.* **2015**, *55*, 552–558. [[CrossRef](#)]
19. Liu, X.; Han, Y.; He, F.; Gao, P.; Yuan, S. Characteristic, hazard and iron recovery technology of red mud—A critical review. *J. Hazard. Mater.* **2021**, *420*, 126542. [[CrossRef](#)]
20. Yang, Y.; Wu, P.; Men, G.; McLean, A. Hot Metal Desulphurization Using Waste Residues from the Aluminum Industry. *High Temp. Mater. Process.* **2012**, *31*, 519–528. [[CrossRef](#)]
21. Bang, K.H.; Kang, Y.B. Recycling Red Mud to Develop a Competitive Desulfurization Flux for Kanbara Reactor (KR) Desulfurization Process. *J. Hazard. Mater.* **2022**, *440*, 129752. [[CrossRef](#)] [[PubMed](#)]
22. Jeong, T.S.; Park, J.H. Effect of Fluorspar and Industrial Wastes (Red Mud and Ferromanganese Slag) on Desulfurization Efficiency of Molten Steel. *Metall. Mater. Trans. B* **2020**, *51*, 2309–2320. [[CrossRef](#)]
23. Zhang, Y.; Li, F.; Wang, R.; Tian, D. Application of Bayer Red Mud-Based Flux in the Steelmaking Process. *Steel Res. Int.* **2017**, *88*, 1600140. [[CrossRef](#)]
24. Li, F.; Zhang, Y.; Guo, Z. Pilot-Scale Test of Dephosphorization in Steelmaking Using Red Mud-Based Flux. *JOM* **2017**, *69*, 1624–1631. [[CrossRef](#)]
25. Zhang, Y.; Li, F.; Yu, K. Using Red Mud-based Flux in Steelmaking for High Phosphorus Hot Metal. *ISIJ Int.* **2018**, *58*, 2153–2155. [[CrossRef](#)]
26. GB/T 20412-2021; Fused Calcium Magnesium Phosphate Fertilizer. Standardization Administration of China: Beijing, China, 2021.
27. Wu, W.; Zhao, B.; Zhao, B.; Wu, W.; Meng, H.D. Hot metal dephosphorization process using calcium ferrite slag without fluorite. *Ironmak. Steelmak.* **2022**, *49*, 661–668. [[CrossRef](#)]
28. Sun, J.; Liu, C.; Jiang, M. Design of Red Mud-based Desilicization and Dephosphorization Flux and Its Application in Ferromanganese. *ISIJ Int.* **2021**, *61*, 1835–1841. [[CrossRef](#)]
29. Jung, I.H.; Van Ende, M.A. Computational Thermodynamic Calculations: FactSage from CALPHAD Thermodynamic Database to Virtual Process Simulation. *Metall. Mater. Trans. B* **2020**, *51*, 1851–1874. [[CrossRef](#)]
30. Kitamura, S.Y. Dissolution Behavior of Lime into Steelmaking Slag. *ISIJ Int.* **2017**, *57*, 1670–1676. [[CrossRef](#)]
31. Vieira, L.M.; Oliveira, H.C.C.d.; Telles, V.B.; Junca, E.; Vieira, E.A.; Oliveira, J.R.d. Influence of Lime Particle and Slag Properties on Lime Dissolution in BOF Converter. *J. Mater. Res. Technol.* **2020**, *9*, 14878–14886. [[CrossRef](#)]
32. Hamano, T.; Horibe, M.; Ito, K. The Dissolution Rate of Solid Lime into Molten Slag Used for Hot-Metal Dephosphorization. *ISIJ Int.* **2004**, *44*, 263–267. [[CrossRef](#)]

Disclaimer/Publisher's Note: The statements, opinions and data contained in all publications are solely those of the individual author(s) and contributor(s) and not of MDPI and/or the editor(s). MDPI and/or the editor(s) disclaim responsibility for any injury to people or property resulting from any ideas, methods, instructions or products referred to in the content.